Research Square

Preprints are preliminary reports that have not undergone peer review.
They should not be considered conclusive, used to inform clinical practice,
or referenced by the media as validated information.

Graben unloading, regional extension and magma viscosity as controls on dike paths and vent locations: numerical models applied to the Hat Creek Graben, California

Khaled Rahimi

kemrahimi@kau.edu.sa

King Abdulaziz University

Research Article

Keywords: Dike propagation, Graben, Vent location, Magma viscosity, Boundary element method, Hat Creek

Posted Date: November 18th, 2026

DOI: https://doi.org/10.21203/rs.3.rs-11578982/v1

License: This work is licensed under a Creative Commons Attribution 4.0 International License.
Read Full License

Additional Declarations: No competing interests reported.

Graben unloading, regional extension and magma viscosity as controls on dike paths and vent locations: numerical models applied to the Hat Creek Graben, California

Khaled Rahimi [1,2]✉

[1] The School of Mines, Department of Earth Sciences and Geophysics, King Abdulaziz University, Bld. A50, P.O.Box 80200, Jeddah, 21589, Kingdom of Saudi Arabia

[2] Geohazards Research Center, Bld. 75, P.O.Box 7863, Jeddah, 22254, Kingdom of Saudi Arabia

✉ kemrahimi@kau.edu.sa

Abstract

Grabens unload the crust and can steer ascending dikes away from their axis, but what controls whether a dike erupts on the graben floor, at the bounding scarps or beyond them remains debated. I used a two-dimensional, plane-strain model of magma-driven dike propagation, coupling linear elastic fracture mechanics with viscous lubrication flow, to simulate basaltic, basaltic-andesitic and andesitic dikes beneath a 0.5-km-deep graben inspired by the Hat Creek Graben, California. Dikes were injected singly, sequentially or simultaneously in four boundary-condition and reference-state configurations, with and without regional extension. The reference state dominated the results. In a gravity-loaded crust, all dikes erupted on the graben floor. In a lithostatic crust, the graben unloading deflected all dikes outwards, to vents 8–18 km from the axis. Regional extension progressively reduced the deflection, and 10 MPa, comparable to the unloading pressure, returned all vents to the graben floor. For dikes fed at a constant supply rate, higher viscosity, fracture toughness and supply rate reduced the deflection. For dikes fed by a reservoir at fixed pressure, viscosity mainly controlled the propagation time. Buoyancy had little effect. Viscosity therefore does not explain the scarp-aligned basaltic andesites of the Hat Creek Graben, which more likely reflect off-axis sources, a lower deviatoric stress during their eruption, or capture by faults. Neighbouring dikes repelled each other by a few hundred metres in a crust with large deviatoric stress, but merged at depth in a lithostatic crust. Vent location beneath grabens is primarily a record of the regional stress state.

Keywords: Dike propagation; Graben; Vent location; Magma viscosity; Boundary element method; Hat Creek

Introduction

Grabens and rift valleys unload the crust beneath them. The unloading rotates the principal stresses, so that beneath the graben floor the maximum compressive stress, σ_1, becomes sub-horizontal and perpendicular to the graben axis, whereas at depth and beneath the flanks it remains closer to vertical (Maccaferri et al. 2014). Because dikes open against the minimum compressive stress, σ_3, and tend to propagate in the plane normal to it, this stress rotation can steer ascending dikes away from the graben axis and towards, or beyond, the bounding fault scarps. Numerical models of crustal-scale rifts (Maccaferri et al. 2014) and normal fault scarps (Maccaferri et al. 2015), and analog experiments with unloading topography (Corbi et al. 2016; Gaete et al. 2019; Rahimi et al. 2025), show that this mechanism can explain the off-axis volcanism observed in many extensional settings. As a rift basin deepens, the same stress rotation can shift volcanism from the basin floor to its flanks (Ferrante et al. 2024).

Whether a particular dike follows the rotated stress field depends on how strongly the magma pressure loads the dike tip relative to the external stress acting on the dike. Maccaferri et al. (2019) showed that the sensitivity of a fluid-filled crack to an external stress field is controlled by the ratio of the external stress to the fluid overpressure and by the crack length. Magma viscosity and density both enter this balance. Viscous flow requires a pressure gradient along the dike, which raises the pressure near the source and changes its distribution (Lister and Kerr 1991; Rubin 1995; Rivalta et al. 2015), whereas the density contrast with the host rock sets the buoyancy that drives the dike upwards. Models that couple fracturing at the tip with viscous flow in the dike (Furst et al. 2023), and their comparison with gelatin experiments (Furst et al. 2024), showed that viscous dissipation controls dike shape and velocity. The effect of

viscosity on the path of dikes that are continuously fed from a source, and that ascend beneath unloading topography, is less well constrained.

The Hat Creek Graben (HCG), northern California, is a natural example where magma composition and vent position are linked. The graben is 4–12 km wide and has a topographic relief of up to ~0.5 km (Muffler et al. 1994; Langenheim et al. 2016). Low-viscosity tholeiitic basalts erupted from vents on the graben floor, with fissures oblique to the graben axis, whereas higher-viscosity calc-alkaline basaltic andesites erupted from vents aligned along the graben-bounding fault scarps (Rahimi and Bursik 2025). Gelatin experiments designed as an analog of the HCG reproduced a similar contrast between water and a more viscous xanthan gum solution (Rahimi et al. in review). The experiments, however, raised several questions. (1) The stress state of the host depends on the boundary conditions and on the assumed reference state, and the fixed walls of the experimental tank may introduce artefacts. (2) The experiments did not include regional extension, which is expected to stabilise graben-parallel dikes in an active graben. (3) It is not clear whether the contrast between magmas is caused by viscosity, by buoyancy, or by small asymmetries in the initial geometry of the dike. (4) The influence of a second dike, propagating at the same time or after the first, remains to be quantified.

Here I address these questions at natural scale with a two-dimensional, plane-strain numerical model of magma-driven dike propagation beneath a Hat Creek-like graben. The model couples linear elastic fracture mechanics with viscous lubrication flow, is fed at a constant magma supply rate, and is embedded in a finite crustal section whose stress state is computed for four boundary-condition and reference-state configurations, with and without regional extension. I simulate basaltic, basaltic-andesitic and andesitic dikes, injected singly, sequentially or simultaneously beneath the graben axis and its flank, and test the sensitivity of the results to the initial dike

orientation, viscosity, density, fracture toughness, supply rate and numerical resolution. The results show when graben unloading controls vent location, when magma properties matter, and how strongly the background stress state and neighbouring dikes modify these outcomes.

Methods

Model geometry and material properties

The model is a two-dimensional, plane-strain vertical section perpendicular to the graben axis (x horizontal, z vertical; Fig. 1a). The reference domain is 40 km wide and 15 km deep. A symmetric graben is cut into its upper surface. The graben is 0.5 km deep, has a flat floor 4 or 8 km wide, and is bounded by scarps dipping 30°. The two floor widths correspond to the southern and central parts of the HCG (Rahimi and Bursik 2025). The crust is homogeneous, isotropic and linear elastic, with density $\rho_r = 2700$ kg m^{-3}, Young's modulus E = 10 GPa and Poisson's ratio $\nu = 0.25$ (Table 1). The effective fracture toughness is $K_c = 100$ MPa m$^{1/2}$. This value lies within the range inferred for dikes at field scale, which is much larger than laboratory values of ~1 MPa m$^{1/2}$ (Delaney and Pollard 1981; Rivalta et al. 2015; Furst et al. 2023). It was varied between 10 MPa m$^{1/2}$ and 1000 MPa m$^{1/2}$ in sensitivity tests.

Three magmas were considered (Table 1): basalt (density $\rho_m = 2650$ kg m^{-3}, viscosity $\mu = 10^2$ Pa s), basaltic andesite (2550 kg m^{-3}, 10^3 Pa s) and andesite (2450 kg m^{-3}, 10^5 Pa s). The viscosities are representative of crystal-poor magmas of these compositions near their liquidus (Lesher and Spera 2015) and of the values adopted for the HCG basalts and basaltic andesites (Rahimi et al. in review). Each magma was treated as an incompressible Newtonian fluid. To separate the effects of viscosity and buoyancy, additional runs varied the viscosity from 10 to 10^6 Pa s at a

fixed density of 2650 kg m^{-3}, and the density from 2450 to 2650 kg m^{-3} at a fixed viscosity of 10^3 Pa s.

Background stress and boundary conditions

The pre-intrusive stress in the crustal section was computed with the finite-element method (quadratic triangular elements refined towards the graben; scikit-fem, Gustafsson and McBain 2020) for the four configurations used to assess the experimental stress field (Rahimi et al. in review, Supplementary Material S3):

(i) zero displacement on the floor and lateral walls, with the stress generated by the self-weight of the crust ("gravity loading");

(ii) frictionless (roller) walls and floor, gravity loading;

(iii) zero displacement on the floor and walls, with a lithostatic initial stress, $\sigma = -\rho_r g d I$, where d is the depth below the reference surface, and with the graben faces unloaded (traction-free). This is the standard reference state for crustal-scale dike models (e.g. Maccaferri et al. 2014; Rivalta et al. 2015);

(iv) a domain three times wider (120 km), with roller boundaries and gravity loading.

In all configurations the top surface, including the graben, is traction-free. With $\nu = 0.25$, gravity loading under lateral confinement produces a horizontal stress equal to $\nu/(1-\nu) \approx 1/3$ of the vertical stress at depth (configurations i, ii and iv), whereas configuration (iii) is isotropic at depth. The four configurations therefore bracket the reference state of the crust, and their comparison shows how strongly the assumed boundary conditions control the results. Regional extension was added to the lithostatic reference state as a uniform horizontal tension, $\Delta\sigma = 1$, 2, 5 or 10 MPa, applied to the lateral boundaries of a 120-km-wide domain. The resulting

perturbation, including the stress concentration at the graben, was computed separately with a roller floor and added to the lithostatic solution. Tensile stresses are positive throughout.

Dike model

Each dike is a fluid-filled crack that is fed at a constant supply rate from a fixed inlet and grows upwards from its upper tip. The elastic problem was solved with the displacement discontinuity method (Crouch and Starfield 1983), using constant-displacement elements 100 m long along the dike. The boundaries of the crustal section were discretised with the same method (element lengths from 150 m near the graben to 1.5 km far from it) and assigned homogeneous conditions consistent with each configuration. The free surface is traction-free. Fixed walls have zero displacement, and roller walls have zero normal displacement and zero shear traction. The opening and slip of the dike are then the response to the fluid pressure, p, acting against the background stress resolved on the dike plane, plus the zero-shear-traction condition on the dike walls. The boundary unknowns were condensed out, so that the effect of the free surface, including the graben topography, and of the lateral boundaries is included in the dike's elastic compliance.

Magma flow along the dike follows lubrication theory:

$$q = -\frac{w^3}{12\mu}\left(\frac{\partial p}{\partial s} + \rho_m g \frac{\partial z}{\partial s}\right), \qquad \frac{\partial w}{\partial t} + \frac{\partial q}{\partial s} = 0,$$

where q is the flux per unit dike breadth, w the dike opening, s the distance along the dike and g the gravitational acceleration. A constant flux, $q_0 = 1$ m^2 s^{-1}, enters at the lower end of the dike, and the flux vanishes at the upper tip (no fluid lag). The value of q_0 corresponds to a volumetric supply of 10^3 m^3 s^{-1} for a dike 1 km in breadth. It was varied between 0.1 and 10 m^2 s^{-1} in

sensitivity tests. A constant flux represents a dike fed at a rate set by the supply from depth. To test the alternative end-member, a dike fed by a reservoir held at constant pressure (Mériaux and Lister 2002; Blackstone et al. 2024), additional runs imposed a fixed magma pressure at the inlet, equal to the lithostatic stress plus an overpressure $\Delta P = 5$ or 10 MPa. The coupled elasticity–lubrication equations were integrated implicitly in time, with Picard iterations on the nonlinear flow conductance.

The dike propagates by one element whenever the mode I stress intensity factor at the tip, K_I, reaches K_c. K_I and the mode II stress intensity factor, K_{II}, are obtained from the opening and slip of the tip element, with a correction factor calibrated against the analytical solution for a pressurised crack. The direction of growth follows the maximum hoop stress criterion (Erdogan and Sih 1963):

$$\theta = 2\arctan\left[\frac{K_I - \sqrt{K_I^2 + 8K_{II}^2}}{4K_{II}}\right],$$

limited to 30° per element. A dike is considered to erupt when its tip reaches the free surface. In three dikes, the tip stalled 30–70 m below the surface, a distance smaller than one element; these dikes were also counted as erupted, at the position of the tip. A dike is arrested if it reaches a lateral or basal boundary, intersects another dike, or fails to reach the surface within ~1 year of model time.

Each dike starts as a 500-m-long starter dike whose lower end is 10 km below the reference surface. The central dike lies beneath the graben axis, and the offset dike 6 km away from it, beneath the graben flank. A perfectly vertical central dike in a symmetric graben cannot leave the axis, because the shear stress on its plane is zero by symmetry. The vertical position is, however,

161 an unstable equilibrium, and any asymmetry (e.g. a slightly oblique feeder, an off-axis source or
162 heterogeneity) may initiate deflection. To represent such asymmetries, the central starter dike
163 was tilted by $\theta_0 = 1°$ towards the offset dike. The effect of this choice was tested with $\theta_0 = 0$, 0.5,
164 2 and 5°.

165 **Injection scenarios**

166 For each configuration and graben width, I simulated single central dikes and single offset dikes
167 of each magma, and pairs of dikes injected either sequentially or simultaneously. In sequential
168 runs, the offset dike was injected after the central dike had erupted. The central dike was kept
169 open, with the opening and slip reached at the time of eruption, so that the stress it imposes on
170 the crust acted on the offset dike. In simultaneous runs, both dikes were injected at the same time
171 and interacted elastically throughout their propagation. Pairs consisted of the same magma
172 (basalt–basalt, basaltic andesite–basaltic andesite, andesite–andesite) or of a central basaltic dike
173 with an offset basaltic andesite or andesite dike, as in the HCG analog experiments. Additional
174 runs used the 120-km-wide domain with a lithostatic reference state, to test the influence of the
175 lateral boundaries in configuration (iii), and regional extension (see above). In total, 247
176 simulations were performed (Supplementary Table S1).

177 **Dimensionless toughness**

178 The relative importance of fracture toughness and viscous flow was quantified with the
179 dimensionless toughness of a plane-strain hydraulic fracture (Detournay 2016),

180 $$\mathcal{K}_m = \frac{K'}{(E'^3 \mu' q_0)^{1/4}}, \qquad K' = 4\sqrt{\frac{2}{\pi}} K_c, \quad E' = \frac{E}{1-\nu^2}, \quad \mu' = 12\mu.$$

Propagation is toughness-dominated for $\mathcal{K}_m \gtrsim 4$ and viscosity-dominated for $\mathcal{K}_m \lesssim 1$ (Detournay 2016). For the reference parameters, $\mathcal{K}_m \approx 1.6$ for basalt, 0.9 for basaltic andesite and 0.3 for andesite (Table 1). All three magmas therefore propagate in the transitional to viscosity-dominated regime that has been inferred for many natural dikes (Rivalta et al. 2015; Furst et al. 2024).

Verification

The model was verified against analytical solutions (Supplementary Material S1). The opening of a uniformly pressurised crack is reproduced to within ~1% at its centre and ~4% on average. The growth of a fluid-driven plane-strain crack in the toughness-dominated limit matches the analytical solution to within 1%. In the viscosity-dominated limit, the crack length is overestimated by ~8% with 100-m elements and ~12% with 200-m elements, and the error decreases with element size. This reflects the limited resolution of the near-tip viscous boundary layer by constant elements. In a uniform stress field with σ_1 inclined to the starter dike, the dike turns and aligns with σ_1 as expected. Within the graben models, halving or doubling the element length changed the vent positions by ≤0.6 km (Supplementary Material S1). The code, written in Python, is available as Supplementary Material.

Use of generative AI

The numerical code and run were prepared with the assistance of a large language model (Claude, Anthropic). The author designed the study, checked the code against the analytical solutions reported in Supplementary Material S1, verified all results and references, and takes full responsibility for the content."

Results

Pre-intrusive stress beneath the graben

The reference state controls the orientation of σ_1 much more strongly than the graben geometry does (Fig. 1). Under gravity loading (configurations i, ii and iv), the horizontal stress at depth is about one third of the vertical stress. The vertical stress then exceeds the horizontal stress by ~80 MPa at 5 km depth and ~170–190 MPa at 10 km depth beneath the graben axis. With roller boundaries (ii, iv), σ_1 is vertical throughout the section, and the graben unloading makes the horizontal stress slightly tensile (+4 to +5 MPa) 0.6 km below the graben floor. With fixed walls (i), by contrast, the self-weight of the crust hangs on the walls. This "silo" effect produces a horizontal compression of ~23–26 MPa beneath the graben floor and a ~1.5-km-thick near-surface layer in which σ_1 is horizontal across the whole section (Fig. 1b, g). This layer is an artefact of the fixed walls.

In the lithostatic reference state (iii), the only deviatoric stress is that produced by the graben. The unloading of $\rho_r g h \approx 13$ MPa makes σ_1 horizontal beneath the graben floor, with $\sigma_{xx} - \sigma_{zz} \approx -7$ MPa 0.6 km below the floor. Because there is no competing deviatoric stress, σ_1 remains sub-horizontal beneath the graben axis down to the base of the model. There $\sigma_{xx} - \sigma_{zz}$ is still −5 to −7 MPa at 10 km depth, and σ_1 is inclined outwards beneath the graben flanks (Fig. 1d, i). A 120-km-wide domain gives the same stresses to within 0.1 MPa, so this result does not depend on the lateral boundaries. Regional extension progressively restores a vertical σ_1. With $\Delta\sigma = 5$ MPa, the horizontal compression beneath the axis decreases to 1–5 MPa above σ_{zz}, and σ_1 is close to vertical only at ~10 km depth beneath the 4-km-wide graben (Fig. 1f, k). With $\Delta\sigma = 10$ MPa, σ_1 is vertical, or the stress nearly isotropic, along the whole axis of both grabens.

Single dikes in the four boundary-condition configurations

The four configurations produced two distinct outcomes (Fig. 2; Table 2). In all three gravity-loaded configurations, the central dikes of all three magmas rose vertically and erupted on the graben floor, within 0.08 km of the axis. The offset dikes erupted 6.0–6.4 km from the axis, i.e. almost vertically above their source. The fixed walls of configuration (i) changed the time to eruption (~170–180 h, compared with ~117–136 h with roller walls) but not the vent positions. These dikes were, however, very wide. Because the horizontal stress at depth is only one third of the vertical stress, the magma pressure needed to reach the surface opened the lower part of the dikes by 72–134 m.

In the lithostatic configuration (iii), all dikes were deflected outwards and erupted beyond the graben shoulders. For the 4-km-wide floor, the central basaltic and basaltic-andesitic dikes turned within ~1 km of their starting depth and erupted 15.8 and 14.4 km from the axis, and the andesitic dike erupted 7.9 km from the axis. For the 8-km-wide floor, the corresponding distances were 18.4, 16.3 and 12.1 km. The offset dikes also migrated outwards, to 10.7–16.8 km from the axis. The 120-km-wide lithostatic domain reproduced these vent positions to within 0.4 km (Table 2), so the deflection is caused by the graben unloading and not by the lateral boundaries. The central dikes reached the surface in 14–47 h. All dikes in this configuration were 2–15 m wide, and the andesitic dikes were the widest.

Effect of regional extension

Regional extension reduced the deflection systematically (Fig. 3). For the 4-km-wide floor and the lithostatic reference state:

- $\Delta\sigma$ = 1 MPa: vents of the central basaltic, basaltic-andesitic and andesitic dikes 10.4, 10.0 and 5.3 km from the axis;
- $\Delta\sigma$ = 2 MPa: 8.2, 7.9 and 3.2 km (the andesitic dike erupted on the opposite side of the graben from the starter-dike tilt);
- $\Delta\sigma$ = 5 MPa: 4.6, 4.3 and 1.7 km. The andesitic dike erupted on the graben floor, and the basaltic and basaltic-andesitic dikes erupted ~1.5 km beyond the graben shoulder (2.9 km from the axis);
- $\Delta\sigma$ = 10 MPa: all three erupted on the graben floor, 0.2–0.4 km from the axis.

The wider graben required more extension to keep dikes within it. With the 8-km-wide floor and $\Delta\sigma$ = 5 MPa, the basaltic and basaltic-andesitic dikes erupted 7.7 and 7.4 km from the axis, beyond the shoulder at 4.9 km, whereas the andesitic dike erupted on the scarp (4.3 km). With $\Delta\sigma$ = 10 MPa, all three erupted on the floor, 0.5–1.0 km from the axis. Extension also shortened the time to eruption, e.g. from 15 to 3 h for the central basaltic dike beneath the 4-km-wide floor.

Effect of magma viscosity, density, fracture toughness and supply rate

In every configuration in which dikes were deflected, the andesitic dikes were deflected less than the basaltic and basaltic-andesitic dikes (Figs. 2, 3). Runs in which viscosity and density were varied independently show that this difference is controlled by viscosity (Fig. 4). At a fixed density of 2650 kg m^{-3}, the vent of the central dike moved from 16.8 km to 0.6 km from the axis as the viscosity increased from 10 to 10^6 Pa s. The decrease was gradual up to 10^4 Pa s (16.8, 15.8, 14.7 and 12.0 km for μ = 10, 10^2, 10^3 and 10^4 Pa s) and steep for higher viscosities (7.3 km for 10^5 Pa s). With 2 MPa of extension, the same trend appeared at higher viscosities: the vent moved from 8.0 to 2.3 km from the axis as μ increased from 10 to 10^6 Pa s, with little change

below 10^3 Pa s. In contrast, decreasing the magma density from 2650 to 2450 kg m^{-3} at $\mu = 10^3$ Pa s, which increases the density contrast with the crust from 50 to 250 kg m^{-3}, moved the vent by only 0.3 km (Fig. 4b).

Increasing the effective fracture toughness also reduced the deflection (Supplementary Fig. S3a). With K_c = 1000 MPa $m^{1/2}$, the central dikes of all three magmas erupted 6.3–7.7 km from the axis in the lithostatic configuration, compared with 7.6–15.8 km for K_c = 100 MPa $m^{1/2}$. With K_c = 10 MPa $m^{1/2}$, the basaltic and basaltic-andesitic dikes erupted 15–16 km from the axis. A ten-fold higher supply rate (q_0 = 10 m^2 s^{-1}; Supplementary Fig. S3b) reduced the deflection (vents 14.6, 12.1 and 4.0 km from the axis for basalt, basaltic andesite and andesite), and a ten-fold lower rate increased it (16.8, 15.2 and 12.2 km). Both higher viscosity and higher supply rate increase the pressure needed to drive the flow, and both decrease $\mathcal{K}_m$. Both reduce the deflection.

The effect of viscosity depended on how the dike was fed (Table 2). When the magma pressure at the inlet was fixed instead of the flux, viscosity had little influence on the path. With ΔP = 5 MPa, the central basaltic, basaltic-andesitic and andesitic dikes erupted 15.6, 15.1 and 14.8 km from the axis. With ΔP = 10 MPa, they erupted 13.8, 14.2 and 13.6 km from the axis. Viscosity instead controlled the propagation time: with ΔP = 5 MPa, the basaltic dike reached the surface in 11 h and the andesitic dike in ~150 days.

Sensitivity to the initial orientation

In the gravity-loaded configuration (i), the central dikes erupted within 0.1 km of the axis for all starter-dike tilts between 0° and 5° (Fig. 5b). The vertical path is therefore stable when the horizontal stress is much smaller than the vertical stress. In the lithostatic configuration, all dikes

were deflected, including those with a perfectly vertical starter dike, for which only the small numerical asymmetries of the discretisation broke the symmetry (Fig. 5a). The vent distance increased only moderately with tilt, from 14.0 to 16.4 km for basalt and from 3.6 to 10.3 km for andesite between $\theta_0 = 0°$ and 5°. The vertical path beneath the graben axis is thus an unstable equilibrium in the lithostatic state. The direction of deflection is set by the initial asymmetry, but its magnitude is set mainly by the stress field and the magma properties. In two runs (andesite with $\Delta\sigma = 2$ MPa, and with $K_c = 10$ MPa $m^{1/2}$), the dike was deflected to the opposite side of the graben from the starter-dike tilt.

Two-dike interactions

In the gravity-loaded configurations, the first dike modified the path of the second only slightly (Fig. 6; Table 3). In sequential runs, the offset dike propagated in the stress field of the open central dike and erupted up to 0.7 km (0.05–0.7 km) farther from the axis than when injected alone. In simultaneous runs, the two dikes repelled each other. The central dike was pushed away from the offset dike and erupted 0.25–0.65 km on the opposite side of the axis, still on the graben floor. The offset dike erupted 0.15–0.7 km farther out than when alone. These shifts were similar for all magma combinations.

In the lithostatic configuration, both dikes migrated outwards along similar paths, and their interaction depended on the injection sequence (Fig. 6). In sequential runs with the same magma, the offset dike followed the path of the earlier central dike and, in most cases, erupted 0.6–1.3 km beyond it. In two runs it merged with the central dike instead: 0.55 km below the surface for basalt beneath the 8-km-wide floor, and 6.8 km below the surface for basaltic andesite in the 120-km-wide domain. When the offset dike was more viscous than the earlier basaltic central

311 dike, it intersected the central dike and was arrested, at 0.7 km depth for basaltic andesite and at
312 7–8 km depth for andesite. In simultaneous runs, the central dike was deflected towards the
313 offset dike and merged with it at 3–9 km depth in all cases, so that only the offset dike erupted,
314 11–19 km from the axis. Regional extension reduced the tendency to merge. With $\Delta\sigma = 2$ MPa,
315 the simultaneous basalt–basalt pair erupted separately (9.2 and 9.5 km from the axis), but the
316 basaltic central dike of the basalt–basaltic andesite pair still merged with the offset dike 0.75 km
317 below the surface. With $\Delta\sigma = 5$ MPa beneath the 4-km-wide floor, the central basaltic dike
318 erupted 4.6–4.9 km from the axis and the offset dike 7.5–7.7 km from it, in both sequential and
319 simultaneous runs. These positions are within 0.3 km of those of the same dikes injected alone
320 (4.6 and 7.6 km). Andesitic pairs interacted more strongly. In the simultaneous run, the central
321 andesitic dike was pushed across the axis and erupted on the opposite scarp, 2.6 km from the
322 axis, instead of on the floor (1.7 km on the near side when alone). In the sequential run, the offset
323 dike erupted 0.7 km closer to the axis than when alone. With $\Delta\sigma = 2$ MPa, the offset dikes of the
324 pairs erupted 0.2–0.4 km farther out than when injected alone (9.2 km).

325 **Numerical resolution**

326 Halving the element length to 50 m or doubling it to 200 m changed the vent positions of the
327 central basaltic and andesitic dikes in the lithostatic configuration by ≤0.6 km (15.8–16.1 km for
328 basalt, 7.6–8.2 km for andesite). The times to eruption changed by <5% (Supplementary Material
329 S1, Fig. S3c).

Discussion

The reference state of the crust controls whether grabens capture or deflect dikes

The most important result is that the choice of boundary conditions and reference state matters more than any magma property. With gravity loading under lateral confinement, the horizontal stress is $\nu/(1-\nu) \approx 1/3$ of the vertical stress, and the resulting differential stress (~80 MPa at 5 km depth) overwhelms the ~10 MPa perturbation produced by a 0.5-km-deep graben. Dikes then rise vertically and erupt on the graben floor, whatever their composition. Such a stress state, however, implies a ratio of vertical to horizontal stress of ~3. This is comparable to the frictional limit for normal faulting ($\sigma_1/\sigma_3 \approx 3.1$ for a friction coefficient of 0.6; Jaeger et al. 2007), and gravitational loading of this kind is generally not an appropriate reference state for volcanic regions (Grosfils 2007). It also produced dikes 72–134 m wide, far wider than observed dikes, which are typically less than ~10 m wide (Rivalta et al. 2015). At the other extreme, the lithostatic reference state has no deviatoric stress except that produced by the topography. The graben then dominates the stress field down to the depth of the source and deflects every dike, including those injected 6 km from the axis, by 8–18 km. The gravity-loaded configurations are therefore an upper bound on the stabilising effect of regional deviatoric stress, and the lithostatic configuration is a lower bound.

The comparison between configurations (i) and (ii) also confirms that fixed lateral walls introduce artefacts. At natural scale, the fixed walls of configuration (i) generated a horizontal compression of up to ~25 MPa in the upper 1.5 km, across the whole width of the section. The same effect, of much smaller magnitude, was identified in the stress models of the gelatin experiments (Rahimi et al. in review, Supplementary Material S3). In the present models, this

352 artefact did not change the vent positions, because the dikes were already held vertical by the
353 gravitational stress at depth. It would, however, bias models in which the near-surface stress
354 controls the final part of the dike path.

355 Real grabens lie between these end members. They are subject to a regional deviatoric stress
356 whose magnitude depends on the tectonic setting and on the stage of the rifting cycle, and which
357 may be partly relaxed by faulting and diking. The extension runs show that the transition
358 between the two outcomes occurs at deviatoric stresses comparable to the graben unloading
359 itself. For a 0.5-km-deep graben with a 4-km-wide floor, dikes erupted beyond the graben
360 shoulders for $\Delta\sigma \lesssim 2$ MPa, near the shoulders for $\Delta\sigma \approx 5$ MPa, and on the floor for $\Delta\sigma = 10$
361 MPa. A wider graben requires more extension to keep dikes on its floor. This agrees with the
362 scaling of Maccaferri et al. (2014), who showed that off-rift volcanism occurs when the
363 unloading pressure is large compared with the tectonic deviatoric stress, and it answers the
364 question of how much the absence of extension in the analog experiments matters. Without
365 extension, both the experiments and the models represent the upper bound of topography-driven
366 deflection. With a regional deviatoric stress of ~10 MPa, comparable to the unloading pressure ρ_r
367 g h, the graben captures the dikes.

368 **When does magma viscosity matter?**

369 The models show that the effect of magma viscosity on dike paths depends on how the dike is
370 fed. For a dike supplied at a constant rate, a more viscous magma is deflected less. At fixed
371 density, increasing the viscosity from 10 to 10^4 Pa s moved the vent of the central dike by less
372 than 5 km, whereas viscosities of 10^5–10^6 Pa s reduced the deflection by a factor of two to more
373 than ten (Fig. 4). Higher fracture toughness and higher supply rate had the same effect. The

common factor is the magma pressure needed to drive the dike. In the toughness-dominated regime, this pressure is set by K_c and the dike length. In the viscosity-dominated regime, it is set by the viscous pressure drop along the dike, which increases with viscosity and supply rate (Lister and Kerr 1991; Detournay 2016). At a fixed supply rate, the net pressure near the source of the andesitic dike (~18 MPa) was about five times that of the basaltic dike (~3 MPa; Fig. 7). A higher internal pressure makes the dike less sensitive to the external stress, as shown by Maccaferri et al. (2019). This is consistent with the general finding that deflection depends on the ratio between the magma driving pressure and the topographic stress perturbation (Corbi et al. 2016; Pinel et al. 2017; Maccaferri et al. 2014, 2019). In contrast, for a dike fed by a reservoir at fixed pressure, the driving pressure does not increase with viscosity. In that case, the three magmas followed nearly the same path, and viscosity mainly controlled the propagation time. Earlier studies did not resolve this dependence. The models of Pinel et al. (2017) computed the trajectory independently of the flow, and Mériaux and Lister (2002) and Blackstone et al. (2024) considered dikes fed by a pressurised chamber, in which viscous pressure losses along the dike reduce the pressure at the tip and enhance the curvature of dike paths. The present results therefore do not support a general rule that more viscous magmas are deflected more or less. The outcome depends on whether the magma supply or the source pressure is fixed, and on the dike's position in the toughness–viscosity regime. Buoyancy had a smaller effect in these models: a five-fold increase in the density contrast moved the vent by only 0.3 km. This is because the dikes remained connected to their source, so that the pressure needed to drive the flow, rather than buoyancy, controlled the overpressure.

This result qualifies the interpretation of the analog experiments that motivated this study. In the experiments, the more viscous xanthan gum dikes deflected towards the graben wall, whereas

water dikes erupted on the graben floor after rotating about a vertical axis (Rahimi et al. in review). A laboratory-scale version of the present model, using the gelatin and fluid properties of the experiments (E = 5 kPa, K_c = 100 Pa $m^{1/2}$, $\mu = 10^{-3}$ and 1 Pa s), placed both fluids in the toughness-dominated regime ($\mathcal{K}_m \approx 30$ and ≈ 6). In that version, water and xanthan gum dikes followed the same paths: vents 5.7 and 5.6 cm from the axis beneath a 4-cm-wide floor, and 9.2 and 9.4 cm beneath an 8-cm-wide floor, with fixed walls (Supplementary Material S2). Because the experiments, like these runs, were fed at a constant flux, the contrast between the experimental fluids is not explained by viscosity alone in two dimensions. Rather, it probably reflects three-dimensional effects that a plane-strain model cannot capture. The different breadth-to-length ratios of the two fluids' dikes also change their elastic compliance. Furst et al. (2024) similarly found that, in gelatin, viscous oil-filled cracks deflected beneath a surface load in a similar way to air-filled cracks.

Implications for the Hat Creek Graben

At the HCG, basaltic vents lie on the graben floor, at normalised distances $\Delta x/G_w \approx 0.003$–$0.19$, whereas basaltic-andesitic vents lie along the bounding scarps, at $\Delta x/G_w \approx 0.5$ (Rahimi and Bursik 2025). In the models with $\Delta\sigma$ = 10 MPa, all central dikes erupted at $\Delta x/G_w = 0.05$–0.12, consistent with the basaltic vents. The scarp position of the basaltic andesites, however, is not reproduced by any model in which the two magmas share a source beneath the graben axis. Where the models predict a difference between magmas, the more viscous magma erupts closer to the axis (Fig. 8), and with a pressure-controlled source the magmas erupt at similar distances. Three alternative explanations are consistent with the models. First, the basaltic andesites may have risen from sources beneath the graben margins. In all configurations, offset dikes erupted at or beyond their source position, and in the lithostatic and weakly extended cases they were

deflected outwards. Second, the stress state may have differed between the two eruptive episodes. The basaltic andesites are older (77–46 ka; Turrin et al. 2007) than the 24 ka Hat Creek Basalt, and the extension direction of the Hat Creek fault system has rotated over this period (Kattenhorn et al. 2016). A lower deviatoric stress during the basaltic-andesitic episode would favour deflection towards the margins, whereas a higher deviatoric stress at 24 ka would favour eruption on the floor. Third, the graben-bounding faults, which are not included in the models, may have captured the basaltic-andesitic dikes. Faults are mechanical discontinuities that can arrest or redirect dikes independently of the topographic stress (Le Corvec et al. 2013).

Interaction between dikes

The two-dike models show that a dike modifies the path of a neighbour mainly by changing the horizontal stress between them. In a crust with a large horizontal deviatoric stress, this effect is small. Two simultaneous dikes 6 km apart repelled each other by a few hundred metres, and an open dike pushed a later dike outwards by up to 0.7 km. In a crust without regional deviatoric stress, by contrast, dikes injected at the same time converged and merged at depth, and a more viscous dike injected after a basaltic one was arrested where it met the earlier dike. Merging and arrest of this kind may explain why some eruptive fissures are fed by fewer dikes than the number of intrusions inferred from geophysical data. The coexistence of basaltic and basaltic-andesitic vents at the HCG suggests that the two magmas did not share a pathway at shallow depth, which is consistent with a non-negligible deviatoric stress or with spatially separate sources.

Limitations

The models are two-dimensional and represent dikes that are infinitely long parallel to the graben axis. The plane-strain assumption overestimates dike opening. The crust is homogeneous and elastic, without faults, layering or inelastic deformation, and the effective fracture toughness is uncertain by at least an order of magnitude. Magma was treated as an incompressible Newtonian fluid without cooling, solidification or fluid lag. The numerical scheme overestimates propagation velocity in the strongly viscosity-dominated limit, although vent positions converged with mesh refinement. The magma supply was constant, and the source was fixed at 10 km depth. These simplifications affect the absolute vent distances. They are unlikely to change the main conclusions: the dominant role of the reference stress state, the stabilising effect of regional extension and of high magma pressure, and the contrast between repulsion and merging of neighbouring dikes.

Conclusions

1. The reference stress state of the crust, rather than magma properties, determines whether a graben captures or deflects ascending dikes. In a gravity-loaded crust, all dikes erupted on the graben floor. In a lithostatic crust, the unloading of a 0.5-km-deep graben deflected dikes from 10 km depth by 8–18 km.
2. Regional extension of a few MPa progressively stabilises vertical dike paths. Dikes erupted beyond the graben shoulders for $\Delta\sigma \lesssim 2$ MPa, near them for $\Delta\sigma \approx 5$ MPa, and on the floor for $\Delta\sigma = 10$ MPa. A wider graben requires more extension to keep dikes within it. Models and experiments without extension therefore give an upper bound for topography-driven deflection.

3. For dikes fed at a constant supply rate, higher magma viscosity reduced deflection, because the larger pressure needed to drive viscous flow makes the dike less sensitive to the external stress. The effect is modest up to ~10^4 Pa s and strong above 10^5 Pa s, and higher fracture toughness and supply rate have the same effect. For dikes fed by a reservoir at fixed pressure, viscosity had little effect on the path and controlled mainly the propagation time. Buoyancy had little influence on dikes connected to their source.
4. Fixed lateral boundaries generate spurious horizontal compression near the surface. Roller boundaries, a lithostatic reference state or a wide domain should be preferred when modelling topographic stresses.
5. In a crust with large deviatoric stress, simultaneously propagating dikes repel each other and an open dike pushes later dikes outwards by up to 0.7 km. In a lithostatic crust, neighbouring dikes converge and may merge or arrest each other.
6. The basalt-on-floor, basaltic-andesite-on-scarp pattern of the Hat Creek Graben is not explained by magma viscosity alone. It more likely reflects off-axis sources, a lower deviatoric stress during the older basaltic-andesitic episode, or capture of dikes by the graben-bounding faults.

Declarations

Funding: No specific external funding was received for this study.

Competing interests: The authors declare no competing interests.

Author contributions: Khaled Rahimi*:* Conceptualization, Methodology, Data curation, Formal analysis, Investigation, Visualization, Writing – original draft, Writing – review & editing.

Data availability: The simulation results (vent positions, dike paths and summary table) are provided as Supplementary Material.

Code availability: The Python code of the dike-propagation and background-stress models, and the scripts used to produce the figures, are provided as a DOI: https://doi.org/10.5281/zenodo.23845353

References

Blackstone LA, Grossman-Ponemon BE, Heimisson ER, Lew AJ, Segall P (2024) Modeling dike trajectories in a biaxial stress field with coupled magma flow, fracture, and elasticity. Bull Volcanol 86:52. https://doi.org/10.1007/s00445-024-01734-8

Corbi F, Rivalta E, Pinel V, Maccaferri F, Acocella V (2016) Understanding the link between circumferential dikes and eruptive fissures around calderas based on numerical and analog models. Geophys Res Lett 43:6212–6219. https://doi.org/10.1002/2016GL068721

Crouch SL, Starfield AM (1983) Boundary element methods in solid mechanics. George Allen & Unwin, London

Daniels KA, Menand T (2015) An experimental investigation of dyke injection under regional extensional stress. J Geophys Res Solid Earth 120:2014–2035. https://doi.org/10.1002/2014JB011627

Delaney PT, Pollard DD (1981) Deformation of host rocks and flow of magma during growth of minette dikes and breccia-bearing intrusions near Ship Rock, New Mexico. US Geol Surv Prof Pap 1202

Detournay E (2016) Mechanics of hydraulic fractures. Annu Rev Fluid Mech 48:311–339. https://doi.org/10.1146/annurev-fluid-010814-014736

Erdogan F, Sih GC (1963) On the crack extension in plates under plane loading and transverse shear. J Basic Eng 85:519–525. https://doi.org/10.1115/1.3656897

509 Ferrante G, Rivalta E, Maccaferri F (2024) Spatio-temporal evolution of rift volcanism
510 controlled top-down by a deepening graben. Earth Planet Sci Lett 629:118593.
511 https://doi.org/10.1016/j.epsl.2024.118593

512 Furst S, Maccaferri F, Pinel V (2023) Modeling the shape and velocity of magmatic intrusions, a
513 new numerical approach. J Geophys Res Solid Earth 128:e2022JB025697.
514 https://doi.org/10.1029/2022JB025697

515 Furst S, Pinel V, Maccaferri F (2024) Dynamics of magmatic intrusion: what can we learn from
516 the comparison of analog and numerical models? Volcanica 7:67–87.
517 https://doi.org/10.30909/vol.07.01.6787

518 Gaete A, Kavanagh JL, Rivalta E, Hazim SH, Walter TR, Dennis DJ (2019) The impact of
519 unloading stresses on post-caldera magma intrusions. Earth Planet Sci Lett 508:109–121.
520 https://doi.org/10.1016/j.epsl.2018.12.016

521 Grosfils EB (2007) Magma reservoir failure on the terrestrial planets: assessing the importance
522 of gravitational loading in simple elastic models. J Volcanol Geotherm Res 166:47–75

523 Gustafsson T, McBain GD (2020) scikit-fem: a Python package for finite element assembly. J
524 Open Source Softw 5:2369. https://doi.org/10.21105/joss.02369

525 Jaeger JC, Cook NGW, Zimmerman RW (2007) Fundamentals of rock mechanics, 4th edn.
526 Blackwell, Oxford

527 Kattenhorn SA, Krantz B, Walker EL, Blakeslee MW (2016) Evolution of the Hat Creek fault
528 system, northern California. In: 3-D structural interpretation: Earth, mind, and machine. AAPG
529 Mem 111. https://doi.org/10.1306/13561990M1113674

Langenheim VE, Jachens RC, Muffler LJP, Clynne MA (2016) Implications for the structure of the Hat Creek fault and transfer of right-lateral shear from the Walker Lane north of Lassen Peak, northern California, from gravity and magnetic data. Geosphere 12:790–808. https://doi.org/10.1130/GES01253.1

Le Corvec N, Menand T, Lindsay J (2013) Interaction of ascending magma with pre-existing crustal fractures in monogenetic basaltic volcanism: an experimental approach. J Geophys Res Solid Earth 118:968–984

Lesher CE, Spera FJ (2015) Thermodynamic and transport properties of silicate melts and magma. In: Sigurdsson H (ed) The encyclopedia of volcanoes, 2nd edn. Academic Press, Amsterdam, pp 113–141

Lister JR, Kerr RC (1991) Fluid-mechanical models of crack propagation and their application to magma transport in dykes. J Geophys Res 96:10049–10077. https://doi.org/10.1029/91JB00600

Maccaferri F, Acocella V, Rivalta E (2015) How the differential load induced by normal fault scarps controls the distribution of monogenic volcanism. Geophys Res Lett 42:7507–7512. https://doi.org/10.1002/2015GL065638

Maccaferri F, Rivalta E, Keir D, Acocella V (2014) Off-rift volcanism in rift zones determined by crustal unloading. Nat Geosci 7:297–300. https://doi.org/10.1038/ngeo2110

Maccaferri F, Smittarello D, Pinel V, Cayol V (2019) On the propagation path of magma-filled dikes and hydrofractures: the competition between external stress, internal pressure, and crack length. Geochem Geophys Geosyst 20:2064–2081. https://doi.org/10.1029/2018GC007915

Mériaux C, Lister JR (2002) Calculation of dike trajectories from volcanic centers. J Geophys Res 107(B4)

Muffler LJP, Clynne MA, Champion DE (1994) Late Quaternary normal faulting of the Hat Creek Basalt, northern California. Geol Soc Am Bull 106:195–200

Paguican EMR, Bursik MI (2016) Tectonic geomorphology and volcano-tectonic interaction in the eastern boundary of the southern Cascades (Hat Creek Graben region), California, USA. Front Earth Sci 4:76. https://doi.org/10.3389/feart.2016.00076

Pinel V, Carrara A, Maccaferri F, Rivalta E, Corbi F (2017) A two-step model for dynamical dike propagation in two dimensions: application to the July 2001 Etna eruption. J Geophys Res Solid Earth 122:1107–1125. https://doi.org/10.1002/2016JB013630

Rahimi K, Bursik M (2025) Inferring magma-feeding fracture geometry through morphological analysis: a volcanotectonic study of Hat Creek Graben, California. J Volcanol Geotherm Res 108507

Rahimi K, Bursik M, Kavanagh JL (2025) The influence of graben geometry on dike propagation. J Volcanol Geotherm Res 458:108254

Rahimi K, Bursik M, Kavanagh JL (in review) Experimental investigation of dike propagation influenced by graben topography and magma viscosity using analog modeling. Bull Volcanol

Rivalta E, Taisne B, Bunger AP, Katz RF (2015) A review of mechanical models of dike propagation: schools of thought, results and future directions. Tectonophysics 638:1–42. https://doi.org/10.1016/j.tecto.2014.10.003

570 Rubin AM (1995) Propagation of magma-filled cracks. Annu Rev Earth Planet Sci 23:287–336.
571 https://doi.org/10.1146/annurev.ea.23.050195.001443

572 Turrin BD, Muffler LJP, Clynne MA, Champion DE (2007) Robust 24 ± 6 ka $^{40}Ar/^{39}Ar$ age of a
573 low-potassium tholeiitic basalt in the Lassen region of NE California. Quat Res 68:96–110

574 Watanabe T, Masuyama T, Nagaoka K, Tahara T (2002) Analog experiments on magma-filled
575 cracks: competition between external stresses and internal pressure. Earth Planets Space
576 54:1247–1261

577

Tables

Table 1 Model parameters. Values in brackets were used in sensitivity tests

Parameter	Symbol	Value
Domain width × depth	W × H	40 × 15 km (120 × 15 km for the wide domain)
Graben depth; scarp dip	h; –	0.5 km; 30°
Graben floor width	G_w	4 km, 8 km
Crustal density	ρ_r	2700 kg m^{-3}
Young's modulus; Poisson's ratio	E; ν	10 GPa; 0.25
Effective fracture toughness	K_c	100 MPa $m^{1/2}$ [10, 1000]
Magma supply per unit breadth	q_0	1 m^2 s^{-1} [0.1, 10]
Source overpressure (pressure-controlled runs)	ΔP	[5, 10 MPa]
Regional extension	Δσ	0 [1, 2, 5, 10 MPa]
Inlet depth; starter-dike length	–	10 km; 0.5 km
Offset of the second dike from the axis	–	6 km
Starter-dike tilt	θ_0	1° [0, 0.5, 2, 5°]
Dike element length	–	100 m [50, 200 m]
Basalt: density, viscosity, $\mathcal{K}_m$	ρ_m, μ	2650 kg m^{-3}, 10^2 Pa s, 1.6
Basaltic andesite: density, viscosity, $\mathcal{K}_m$	ρ_m, μ	2550 kg m^{-3}, 10^3 Pa s, 0.9
Andesite: density, viscosity, $\mathcal{K}_m$	ρ_m, μ	2450 kg m^{-3}, 10^5 Pa s, 0.3
Viscosity sweep (ρ_m = 2650 kg m^{-3})	μ	$10–10^6$ Pa s

Table 2 Distance (km) between the vent of the central dike and the graben axis, for single dikes injected beneath the axis of grabens with 4- and 8-km-wide floors. F: graben floor; S: scarp; O: off-graben (beyond the graben shoulder). Constant-flux source unless stated

Configuration	Basalt, 4 km	Bas. andesite, 4 km	Andesite, 4 km	Basalt, 8 km	Bas. andesite, 8 km	Andesite, 8 km
(i) Fixed walls, gravity loading	0.1 (F)	0.0 (F)	0.0 (F)	0.1 (F)	0.1 (F)	0.0 (F)
(ii) Roller walls, gravity loading	0.0 (F)	0.0 (F)	0.1 (F)	0.0 (F)	0.0 (F)	0.0 (F)
(iv) Wide domain, roller walls, gravity loading	0.0 (F)	0.0 (F)	0.0 (F)	0.0 (F)	0.1 (F)	0.0 (F)
(iii) Fixed walls, lithostatic	15.8 (O)	14.4 (O)	7.9 (O)	18.4 (O)	16.3 (O)	12.1 (O)
(iii) Wide domain, lithostatic	15.8 (O)	14.5 (O)	7.6 (O)	18.4 (O)	16.6 (O)	11.9 (O)
Wide lithostatic + Δσ = 1 MPa	10.4 (O)	10.0 (O)	5.3 (O)	13.5 (O)	12.3 (O)	10.0 (O)
Wide lithostatic + Δσ = 2 MPa	8.2 (O)	7.9 (O)	3.2 (O)	10.9 (O)	10.4 (O)	8.4 (O)
Wide lithostatic + Δσ = 5 MPa	4.6 (O)	4.3 (O)	1.7 (F)	7.7 (O)	7.4 (O)	4.3 (S)
Wide lithostatic + Δσ = 10 MPa	0.3 (F)	0.4 (F)	0.2 (F)	1.0 (F)	0.5 (F)	0.5 (F)

Configuration	Basalt, 4 km	Bas. andesite, 4 km	Andesite, 4 km	Basalt, 8 km	Bas. andesite, 8 km	Andesite, 8 km
Wide lithostatic, pressure-controlled source, ΔP = 5 MPa	15.6 (O)	15.1 (O)	14.8 (O)	–	–	–
Wide lithostatic, pressure-controlled source, ΔP = 10 MPa	13.8 (O)	14.2 (O)	13.6 (O)	–	–	–

583 **Table 3** Outcomes of two-dike runs beneath the graben with a 4-km-wide floor. Vent distances
584 are measured from the graben axis; positive values are on the side of the offset dike. F: graben
585 floor; S: scarp; O: off-graben. "Merged" indicates that the dike intersected the other dike at the
586 depth given and did not erupt separately. The offset dikes injected alone erupted 6.2–6.3 km (i),
587 10.7–15.5 km (iii) and 7.6 km (lithostatic + 5 MPa) from the axis

Configuration	Injection	Central + offset magma	Central dike (km)	Offset dike (km)
(i) gravity loading	sequential	basalt + basalt	+0.1 (F)	+6.9 (O)
(i) gravity loading	sequential	basaltic andesite + basaltic andesite	+0.0 (F)	+6.9 (O)
(i) gravity loading	sequential	andesite + andesite	+0.0 (F)	+6.9 (O)
(i) gravity loading	sequential	basalt + basaltic andesite	+0.1 (F)	+7.0 (O)
(i) gravity loading	sequential	basalt + andesite	+0.1 (F)	+7.0 (O)
(i) gravity loading	simultaneous	basalt + basalt	-0.6 (F)	+6.9 (O)
(i) gravity loading	simultaneous	basaltic andesite + basaltic andesite	-0.6 (F)	+6.8 (O)
(i) gravity loading	simultaneous	andesite + andesite	-0.7 (F)	+6.9 (O)
(i) gravity loading	simultaneous	basalt + basaltic andesite	-0.6 (F)	+6.9 (O)
(i) gravity loading	simultaneous	basalt + andesite	-0.6 (F)	+7.0 (O)
(iii) lithostatic	sequential	basalt + basalt	+15.8 (O)	+16.3 (O)
(iii) lithostatic	sequential	basaltic andesite + basaltic andesite	+14.4 (O)	+15.7 (O)
(iii) lithostatic	sequential	andesite + andesite	+7.9 (O)	+9.1 (O)
(iii) lithostatic	sequential	basalt + basaltic andesite	+15.8 (O)	merged at 0.7 km
(iii) lithostatic	sequential	basalt + andesite	+15.8 (O)	merged at 7.3 km
(iii) lithostatic	simultaneous	basalt + basalt	merged at 5.2 km	+16.6 (O)
(iii) lithostatic	simultaneous	basaltic andesite + basaltic andesite	merged at 5.4 km	+15.6 (O)
(iii) lithostatic	simultaneous	andesite + andesite	merged at 3.3 km	+11.7 (O)

Configuration	Injection	Central + offset magma	Central dike (km)	Offset dike (km)
(iii) lithostatic	simultaneous	basalt + basaltic andesite	merged at 6.6 km	+15.8 (O)
(iii) lithostatic	simultaneous	basalt + andesite	merged at 8.5 km	+12.1 (O)
Wide lithostatic + 5 MPa	sequential	basalt + basalt	+4.6 (O)	+7.5 (O)
Wide lithostatic + 5 MPa	sequential	andesite + andesite	+1.7 (F)	+6.9 (O)
Wide lithostatic + 5 MPa	sequential	basalt + basaltic andesite	+4.6 (O)	+7.5 (O)
Wide lithostatic + 5 MPa	simultaneous	basalt + basalt	+4.9 (O)	+7.7 (O)
Wide lithostatic + 5 MPa	simultaneous	andesite + andesite	-2.6 (S)	+8.1 (O)
Wide lithostatic + 5 MPa	simultaneous	basalt + basaltic andesite	+4.6 (O)	+7.7 (O)

588

589 **Figure captions**

590 **Fig. 1** Model set-up and pre-intrusive stress. **a** Crustal section (to scale) with the graben, the
591 boundary conditions and the inlets of the central and offset dikes. **b–k** Tilt of the maximum
592 compressive principal stress, σ_1, from the vertical (colour) and σ_1 orientation (ticks) beneath
593 grabens with 4-km-wide (b–f) and 8-km-wide (g–k) floors. Columns show the gravity-loaded
594 configurations with fixed walls (i; b, g), roller walls (ii; c, h) and a 120-km-wide domain (iv; e,
595 j), the lithostatic configuration (iii; d, i) and the lithostatic configuration with 5 MPa of regional
596 extension (f, k). Diamonds mark the dike inlets, 10 km below the surface. Only the central 24 km
597 of each section is shown

598 **Fig. 2** Paths of single central dikes of basalt (solid), basaltic andesite (dash-dot) and andesite
599 (dashed) beneath grabens with 4-km-wide (a–d) and 8-km-wide (f–i) floors, in the four
600 boundary-condition configurations. Stars mark vents. **e, j** Depth of the dike tip versus time for
601 the lithostatic configuration (iii; thick lines) and the gravity-loaded configuration with fixed
602 walls (i; thin lines)

603 **Fig. 3** Effect of regional extension on dikes in the lithostatic reference state (120-km-wide
604 domain). **a** Paths of basaltic (solid) and andesitic (dashed) central dikes beneath the graben with
605 a 4-km-wide floor for regional extension $\Delta\sigma$ = 0–10 MPa. **b, c** Distance of the vent from the
606 graben axis versus $\Delta\sigma$ for the 4- and 8-km-wide floors. Green and beige bands mark the graben
607 floor and scarps

608 **Fig. 4** Effect of magma properties on vent position (lithostatic reference state, 120-km-wide
609 domain, 4-km-wide floor). **a** Vent distance versus magma viscosity at a fixed magma density of
610 2650 kg m^{-3}, without extension and with $\Delta\sigma$ = 2 MPa. The upper axis gives the dimensionless

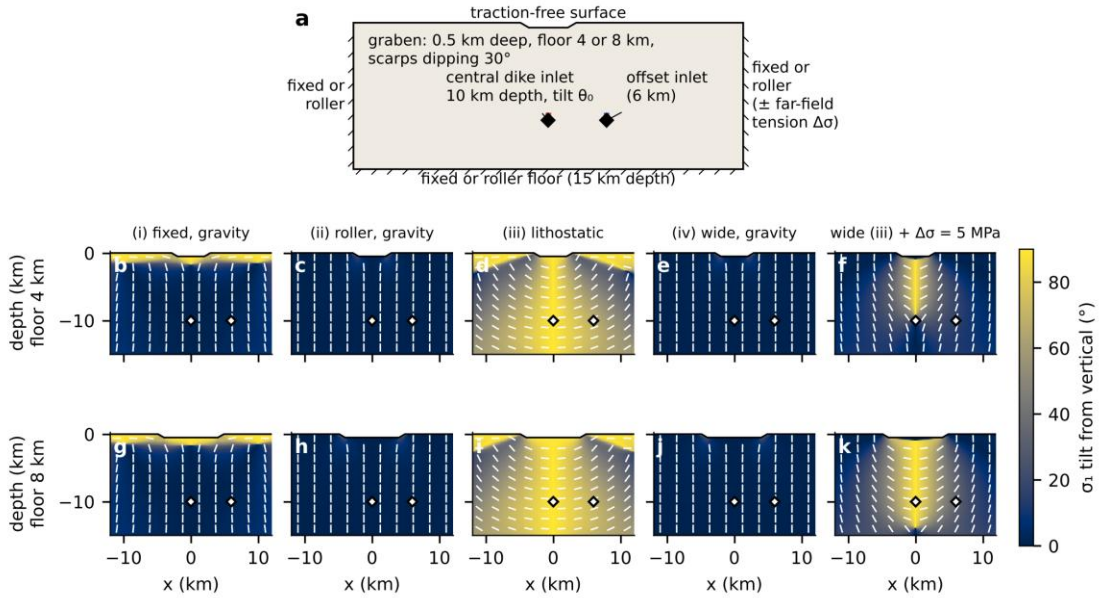
toughness $\mathcal{K}_m$ for $q_0 = 1\ m^2\ s^{-1}$. Dotted lines mark the reference viscosities of basalt, basaltic andesite and andesite. **b** Vent distance versus density contrast between crust and magma at a viscosity of 10^3 Pa s

Fig. 5 Sensitivity of vent position to the tilt of the central starter dike, θ_0, beneath the graben with a 4-km-wide floor: **a** lithostatic reference state (120-km-wide domain); **b** gravity loading with fixed walls (configuration i). Green and beige bands mark the graben floor and scarps

Fig. 6 Paths of pairs of dikes injected sequentially (columns 1–3) or simultaneously (columns 4–6) beneath the graben with a 4-km-wide floor, in the gravity-loaded configuration with fixed walls (a–f), the lithostatic configuration (g–l) and the lithostatic configuration with 5 MPa of regional extension (m–r). Grey lines show the paths of the same dikes injected alone. Stars mark vents, and crosses mark the points where a dike intersected the other dike

Fig. 7 Opening (a) and net pressure (magma pressure minus the normal compressive stress on the dike plane; b) along vertical central dikes 6 km long, fed at a constant flux, beneath the graben with a 4-km-wide floor and 10 MPa of regional extension. The dotted line is for a magma with the viscosity of andesite (10^5 Pa s) and the density of basalt

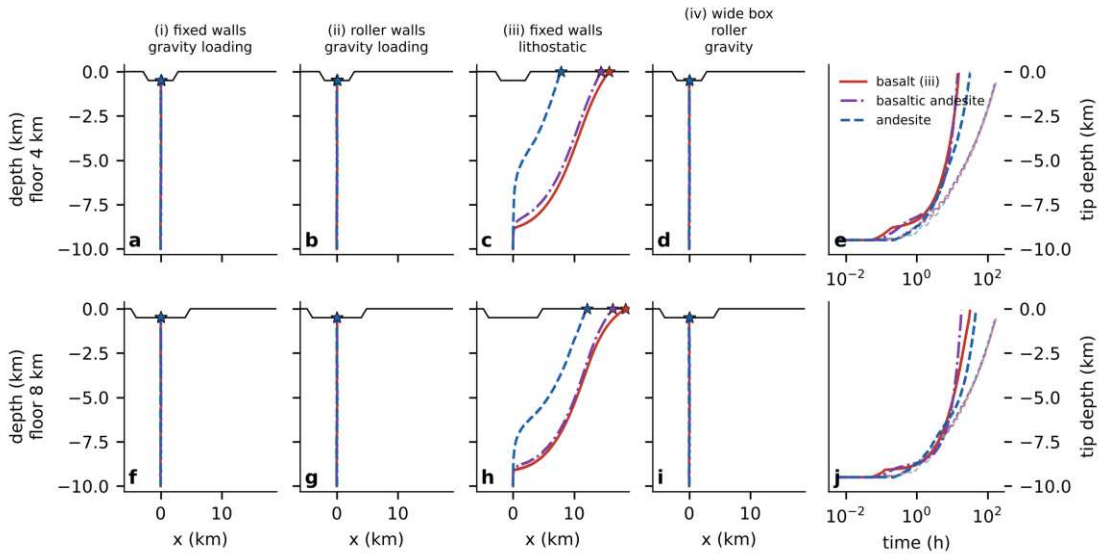
Fig. 8 Vent positions of single central dikes normalised by the graben floor width ($\Delta x/G_w$) for all reference-state configurations and graben widths, compared with the ranges of basaltic ($\Delta x/G_w \approx$ 0.003–0.19; red band) and basaltic-andesitic ($\Delta x/G_w \approx 0.5$; purple line) vents at the Hat Creek Graben (Rahimi and Bursik 2025). The horizontal axis is linear up to 0.5 and logarithmic beyond. Green and beige bands mark the graben floor and scarps



632

633 **Fig. 1**

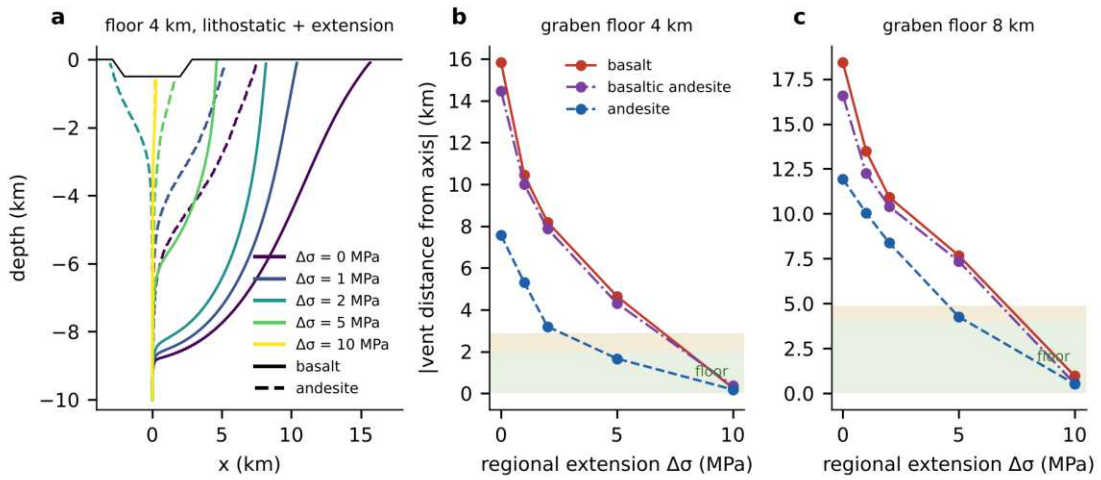
634



635

636 **Fig. 2**

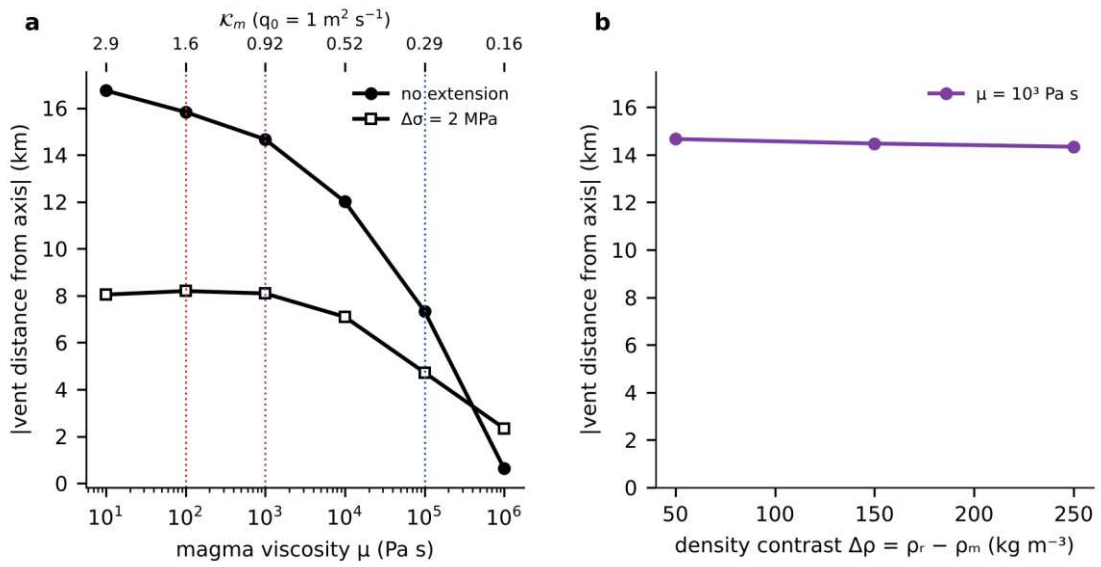
637



638

639 **Fig. 3**

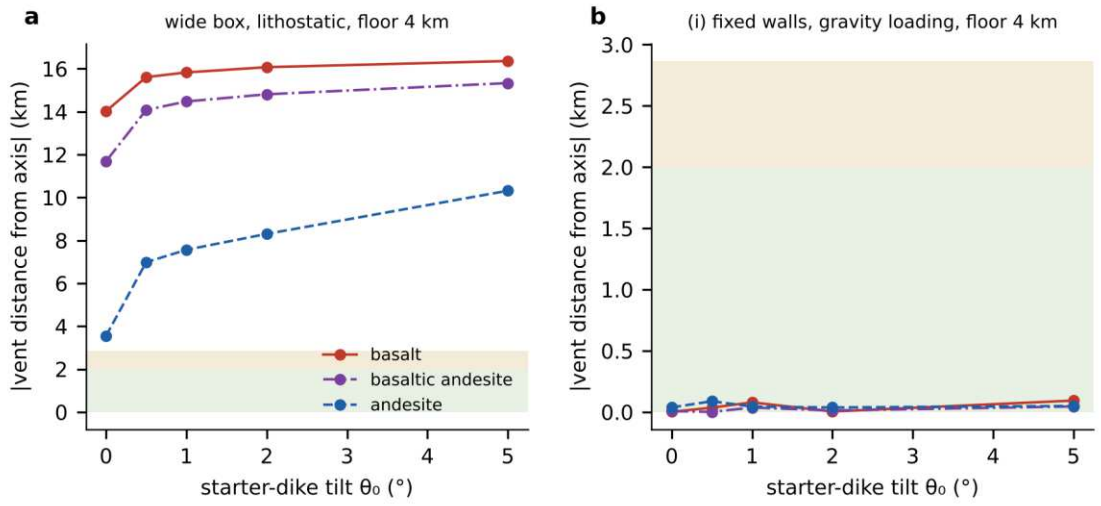
640



641

642 **Fig. 4**

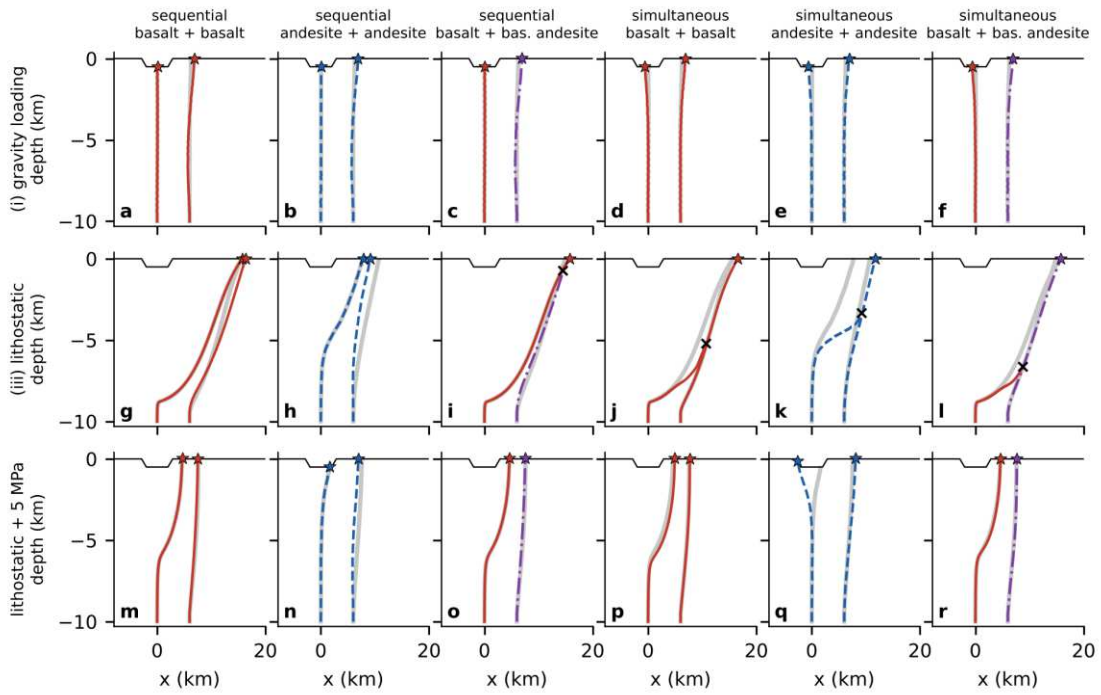
643



644

645 **Fig. 5**

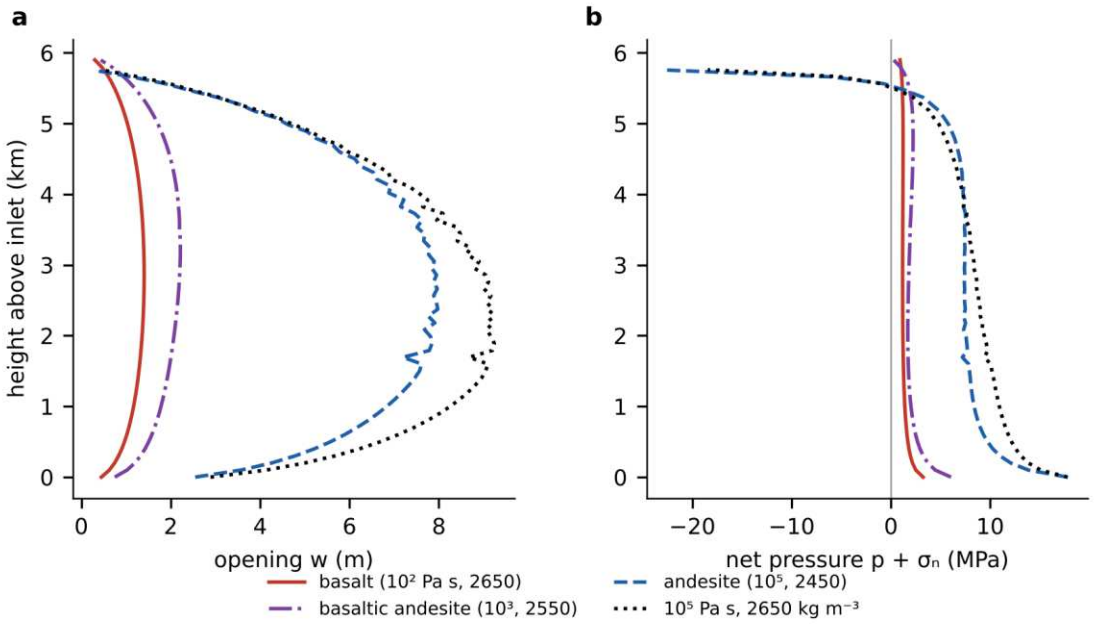
646



647

648 **Fig. 6**

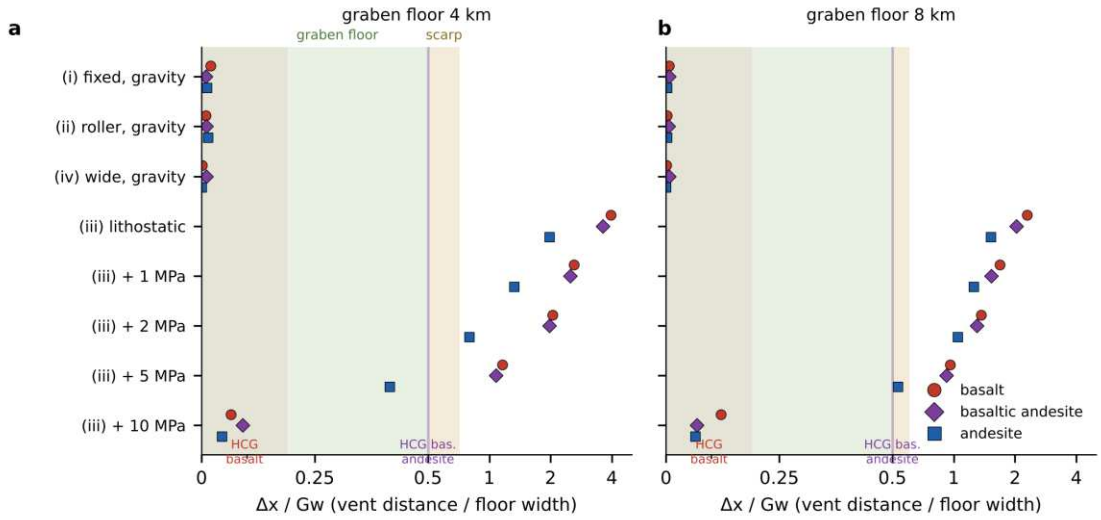
649



650

651 **Fig. 7**

652


a
graben floor 4 km
graben floor
scarp
(i) fixed, gravity
(ii) roller, gravity
(iv) wide, gravity
(iii) lithostatic
(iii) + 1 MPa
(iii) + 2 MPa
(iii) + 5 MPa
(iii) + 10 MPa
HCG basalt
HCG bas. andesite
0
0.25
0.5
1
2
4
Δx / Gw (vent distance / floor width)
b
graben floor 8 km
basalt
basaltic andesite
andesite

653

654 **Fig. 8**

Supplementary Files

This is a list of supplementary files associated with this preprint. Click to download.

- RahimiGrabenDikeNumericalBVSupplementary.docx